Surface Accumulation Induced Negative Schottky Barrier and Ultralow Contact Resistance in Atomic-Layer-Deposited In_2O_3 Thin-Film Transistors

Chang Niu, *Graduate Student Member, IEEE*, Zehao Lin, Vahid Askarpour, Zhuocheng Zhang, Pukun Tan, *Graduate Student Member, IEEE*, Mengwei Si, *Member, IEEE*, Zhongxia Shang, Yizhi Zhang, Haiyan Wang, Mark S. Lundstrom, *Life Fellow, IEEE*, Jesse Maassen, and Peide D. Ye, *Fellow, IEEE*

***Abstract*—As transistor dimensions reach the 3-nm node, interface and surface engineering emerges as critical considerations. Challenges introduced by reduced conductivity and mobility due to surface depletion significantly impact thickness scaling and contact performance. In this work, we report the surface accumulation in atomic layer deposition (ALD) grown In_2O_3 thin-film transistors (TFTs). The negative Schottky barrier enables an ultralow metal-to-semiconductor contact resistance of $R_c = 23.4\ \Omega\,\mu$m at electron charge density $n_{2D} = 5.0 \times 10^{13}$ cm^{-2} in a nanometer ultrathin In_2O_3 channel. The effect of film thickness and annealing on contact resistance is investigated. Ultralow contact resistivity $\rho_c \approx 1.3 \times 10^{-9}\ \Omega\,$cm^2 and current transfer length $L_T \approx 2$ nm are achieved in a 1-nm-thick film. The superior ohmic contact is made possible by the charge neutrality level (CNL) deeply aligned inside the conduction band for In_2O_3. Together with theoretical calculations, the Landauer quantum resistance limit of In_2O_3 is discussed. Furthermore, the ALD-grown In_2O_3 transistor is back-end-of-line (BEOL) compatible with a low thermal budget of 400 °C (even considering the optional O_2 annealing). Our work demonstrates that In_2O_3 is also an up-and-coming candidate for ultra-scaled, high-performance BEOL transistors from even the contact engineering point of view.**

***Index Terms*—Atomic layer deposition (ALD), back-end-of-line (BEOL) compatible, contact resistance, indium oxide, negative Schottky barrier, surface accumulation, thin-film transistor (TFT).**

I. INTRODUCTION

CONTACT engineering between a metal and a semiconductor is one of the most important topics in modern CMOS research as the channel length continuously scales down. In the near ballistic region, the total ON-resistance of a transistor is primarily determined by the contacts. The contact resistance in metal-to-semiconductor junctions typically originates from the Schottky barrier, which is mostly dominated by the so-called Fermi-level pinning. The thermal injection of electrons over the Schottky barrier gives rise to the large contact resistance. Minimizing contact resistance is crucial for the industry to further improve device performance and extend Moore's law.

Recently, there has been significant interest in back-end-of-line (BEOL) device technology for monolithic 3-D integration, especially oxide semiconductor thin-film transistors (TFTs) [1], [2], [3], [4], [5], [6], [7], [8], [9], [10]. Atomic layer deposition (ALD) grown In_2O_3-based semiconducting materials are considered as promising candidates for BEOL channel materials due to their low thermal budget [11], compatibility with large wafer-scale fabrication, high uniformity and conformability, controllable channel thickness [12], controllable element doping, and excellent device performance with a mobility exceeding 100 cm^2/V·s [11], ON-current approaching 20 mA/μm [13], [14], and ultrahigh bias stability [15].

Manuscript received 30 December 2023; revised 12 February 2024; accepted 14 February 2024. Date of publication 26 February 2024; date of current version 24 April 2024. This work was supported in part by the Semiconductor Research Corporation (SRC), in part by the nanoelectronic COmputing REsearch (nCORE) Innovative Materials and Processes for Accelerated Compute Technologies (IMPACT) Center, in part by the Air Force Office of Scientific Research (AFOSR) and SRC/Defense Advanced Research Projects Agency (DARPA) Joint University Microelectronics Program (JUMP) Applications and Systems Driven Center for Energy-Efficient Integrated NanoTechnologies (ASCENT) Center, in part by the Natural Sciences and Engineering Research Council of Canada (NSERC), and in part by the Digital Research Alliance of Canada. This article is an extended version of a paper presented at IEDM 2023. The review of this article was arranged by Editor E. Gnani. *(Corresponding author: Peide D. Ye.)*

Chang Niu, Zehao Lin, Zhuocheng Zhang, Pukun Tan, Mengwei Si, Mark S. Lundstrom, and Peide D. Ye are with the Elmore Family School of Electrical and Computer Engineering, Birck Nanotechnology Center, Purdue University, West Lafayette, IN 47907 USA (e-mail: yep@purdue.edu).

Vahid Askarpour and Jesse Maassen are with the Department of Physics and Atmospheric Science, Dalhousie University, Halifax, NS B3H 4R2, Canada.

Zhongxia Shang, Yizhi Zhang, and Haiyan Wang are with the School of Materials Engineering, Purdue University, West Lafayette, IN 47907 USA.

Color versions of one or more figures in this article are available at https://doi.org/10.1109/TED.2024.3367312.

Digital Object Identifier 10.1109/TED.2024.3367312

0018-9383 © 2024 IEEE. Personal use is permitted, but republication/redistribution requires IEEE permission.
See https://www.ieee.org/publications/rights/index.html for more information.

Authorized licensed use limited to: Purdue University. Downloaded on April 29,2024 at 17:42:21 UTC from IEEE Xplore. Restrictions apply.

In this work, we demonstrated an ultralow contact resistance in ALD In_2O_3 TFTs. In contrast to the positive Schottky barrier induced by the Fermi-level pinning effect in Si or III–V (except for InAs), in In_2O_3, the surface accumulation [16] ensures band bending at the contact, resulting in a negative Schottky barrier, which is experimentally observed. Together with theoretical calculations, the Landauer quantum limit of the contact resistance is discussed.

In the search for new devices to outperform Si MOSFET using novel channel materials, most of the devices are exactually Schottky barrier transistors instead of inversion-mode MOSFET like silicon one, where silicide is employed as source/drain contacts to minimize the contact resistance with silicon channel. The general presence of a positive Schottky barrier in a Schottky barrier transistor induces large contact resistance and restricts its ON-current, subthreshold slope, and other device performance. This is the fundamental reason why a Schottky barrier transistor is hard to exceed Si MOSFET. However, if a negative Schottky barrier was realized as pointed out by [17], negative Schottky barrier contacts would enable gate tuning of a thermionic barrier only as a Si MOSFET. A negative Schottky barrier is crucial for a Schottky barrier transistor to achieve the transistor performance comparable to a ballistic Si MOSFET.

Reducing the contact resistance of the transistor further enables shorter delays in logic applications. Our work provides new insight into designing and engineering new channel materials with distinct surface functions in future electronic devices.

II. EXPERIMENTAL AND COMPUTATIONAL PROCEDURE

Fig. 1(a) shows the schematic of an In_2O_3 transistor. The structure stack includes 40-nm Ni as the bottom gate metal, 3- or 5-nm ALD grown HfO_2 as the gate dielectric, 1–3-nm ALD grown In_2O_3 as the semiconducting channel, and 80-nm Ni as source/drain contact electrodes. Fig. 1(b) presents the fabrication process flow. Fig. 1(c) shows the cross-sectional scanning transmission electron microscopy (STEM) image as well as the energy dispersive X-ray spectroscopy (EDS) elemental mapping of an In_2O_3 TFT.

The device fabrication process started with a p^+ Si substrate with 90-nm thermally grown SiO_2, followed by a standard cleaning process, including ultrasonic rinsing with toluene, acetone, and isopropyl alcohol (IPA) to remove possible organic particles and dirty materials. A standard lift-off process was then applied for the 40-nm Ni bottom gate by electron-beam lithography and evaporation; 3- or 5-nm HfO_2 was deposited by ALD at 200 °C, using $[(CH_3)_2N]_4Hf$ (TDMAHf) and H_2O as Hf and O precursors; 1–3-nm In_2O_3 was deposited by ALD at 225 °C with $(CH_3)_3In$ (TMIn) and H_2O as In and O precursors. TMIn precursor was heated to 60 °C to provide sufficient vapor pressure and N_2 with a flow rate of 40 sccm was used as the carrier gas. The film thickness is accurately controlled by the number of ALD cycles. The thickness of the ALD In_2O_3 film was measured by ellipsometer (Gaertner L116A) and calibrated by transmission electron microscopy (TEM) and atomic force microscope (AFM). Channel isolation was done by wet etching of In_2O_3 using concentrated hydrochloric acid; 80-nm Ni was deposited by electron-beam evaporation as source/drain contacts, patterned by electron-beam lithography with L_{ch} ranging from 40 nm to 1 μm. The fabricated devices were then annealed at various temperatures (190 °C–400 °C) in O_2 atmosphere. The O_2 annealing is optional. Note that the whole process is BEOL compatible with a low thermal budget of 400 °C even considering high-temperature O_2 annealing.

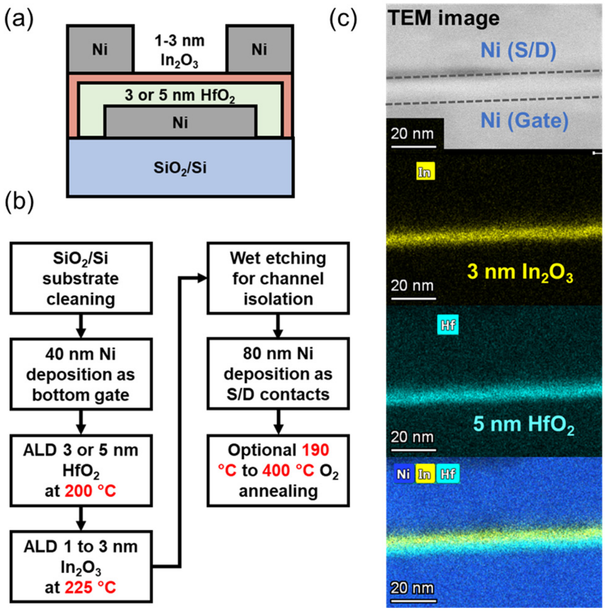

Fig. 1. (a) Schematic device structure of an In_2O_3 bottom-gate TFT. (b) Fabrication process flow with a total thermal budget of 400 °C, ensuring compatibility with BEOL processing, even with optional high-temperature annealing. (c) TEM image verifying the chemical composition and device structure.

The electrical characterization at room temperature (295 K) was performed in a Cascade probe station with the Keysight B1500A system in atmosphere. The temperature-dependent characterization (10–295 K) was performed in a Lakeshore CRX-VF cryogenic probe station. The threshold voltages are determined by the linear extrapolation method based on the transfer characteristics. The carrier density is estimated from the dielectric oxide capacitance measured in experiment and the gate voltage applied. More than 100 devices were measured with similar behavior in this work.

Four In_2O_3 nanometer thin films of thickness equal to 0.95, 1.98, 3.00, and 3.52 nm are simulated with the density-functional theory (DFT) code Quantum Espresso [18]. The top and bottom surfaces are terminated with oxygen atoms, each of which is passivated with a hydrogen atom. All atoms are relaxed to within the energy and force thresholds of 10^{-5} Ry and 10^{-4} Ry/Bohr, respectively. The calculations are performed with a plane-wave energy cutoff of 140 Ry, 3×3 $\mathbf{k}$-grid, Perdew–Burke–Ernzerhof (PBE) exchange-correlation [19], norm-conserving Vanderbilt pseudopotentials [20], and a vacuum region of 25 Å. Using the Wannier90 code [21], the electron eigen-energies and velocities are interpolated onto a fine 200×200 $\mathbf{k}$-grid to compute the distribution of modes.

Authorized licensed use limited to: Purdue University. Downloaded on April 29,2024 at 17:42:21 UTC from IEEE Xplore. Restrictions apply.

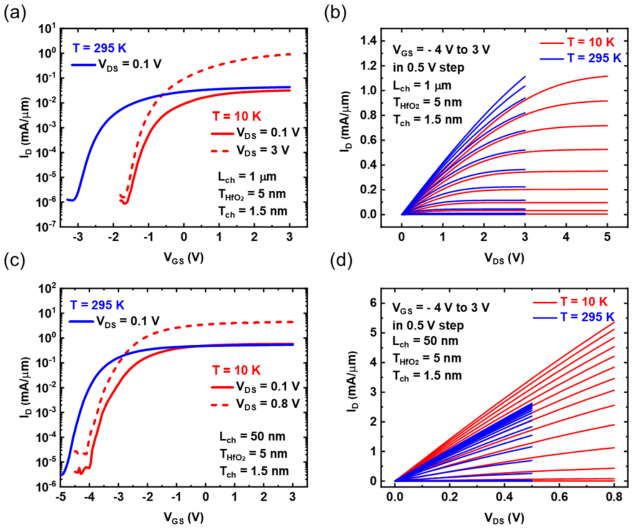

Fig. 2. (a) Transfer and (b) output characteristics of a long-channel In_2O_3 transistor with L_{ch} of 1 μm and T_{ch} of 1.5 nm at 10 K (red) and 295 K (blue). (c) Transfer and (d) output characteristics of a short-channel In_2O_3 transistor with L_{ch} of 50 nm and T_{ch} of 1.5 nm at 10 K (red) and 295 K (blue). A high ON-current of 5.4 mA/μm is achieved.

III. RESULTS AND DISCUSSION

Fig. 2(a) and (b) shows the transfer and output characteristics of a long channel In_2O_3 transistor with L_{ch} of 1 μm and T_{ch} of 1.5 nm at room temperature (295 K, blue) and low temperature (10 K, red). Excellent current saturation is observed at a large V_{DS} when $V_{DS} > V_{GS} - V_T$. The ON-current is slightly decreased at low temperature (10 K) at the same V_{DS} and V_{GS} because the threshold voltage shifted positively (+1.5 V) due to the carrier freezing when the temperature was cooled down. The mobility of the In_2O_3 channel estimated from the field-effect under low temperatures is similar to room temperature due to its amorphous nature. Fig. 2(c) and (d) shows the transfer and output characteristics of a short-channel In_2O_3 transistor with L_{ch} of 50 nm and T_{ch} of 1.5 nm. Larger V_{DS} can be applied due to the reduced self-heating effects (SHE) under low temperatures. A high ON-current of 2.6 mA/μm at 0.5 V under 295 K and 5.4 mA/μm at 0.8 V under 10 K is observed, which is attributed to the high electron charge density and high band velocity of ALD In_2O_3 [13], [14]. Due to the wide bandgap 3.0 eV of In_2O_3, the ON–OFF ratio limited by the measurement equipment remains the same at high temperature. Note that the ON-current increases at low temperatures, accompanied by a positive shift in threshold voltage, contrasting the behavior observed in long-channel devices. This can be explained by the temperature-dependent contact resistance decrease at low temperatures and the charge injection from the contacts due to the surface-accumulation-induced negative Schottky barrier.

The schematic band diagram of ALD-grown In_2O_3 is presented in Fig. 3(a), illustrating the electron density of states at different energies. Three important energy levels are shown: E_F Fermi level, E_c conduction band minimum edge, and E_{CNL} charge neutrality level (CNL). The CNL is characterized by the interfacial trap properties of a material, where the surface states have both acceptor and donor type traps at the same magnitude. The acceptor type trap is negatively charged when full and neutral when empty, while the donor-type trap is neutral when full and positively charged when empty. The CNL arises from interface bonds or surface dangling bonds, which are sensitive to factors, such as decoration, material composition, and surface roughness, giving great potential to engineering electronic properties in various materials. In In_2O_3, the relative positions of these three important energy levels give rise to the surface accumulation and the high ON-current in thin films (1.5 nm). First, the Fermi level is above the conduction band ($E_F > E_c$), making In_2O_3 a degenerate semiconductor. Second, the CNL is above the Fermi surface ($E_{CNL} > E_F$), resulting in the donor-type interfacial trap states, which are positively charged. These trap states mainly originate from the oxygen vacancies, which can be tuned by the post O_2 annealing. Third, the CNL is above the conduction band edge ($E_{CNL} > E_c$), providing available states inside the In_2O_3 channel.

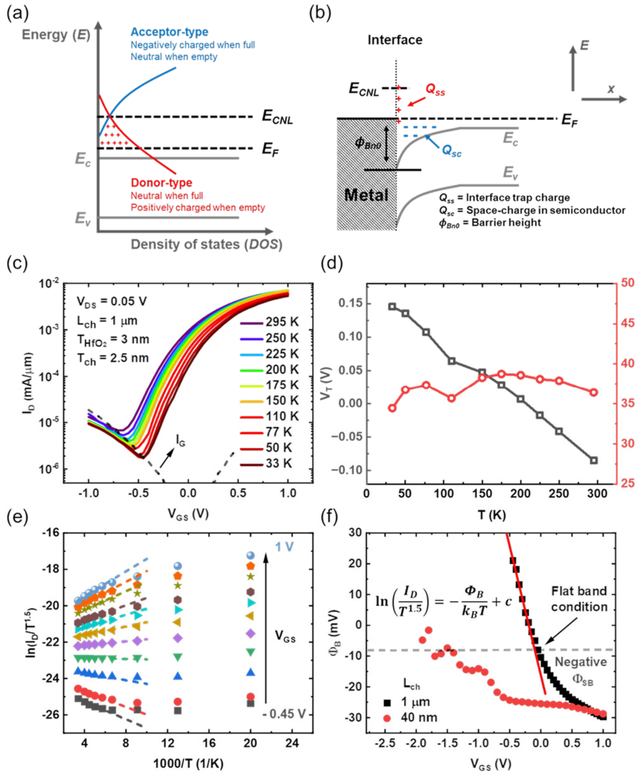

Fig. 3. (a) Schematic of the trap density at the In_2O_3 interface. The CNL E_{CNL} is located deeply inside the conduction band and above the Fermi level E_F, providing positive charges at the In_2O_3 interface. (b) Schematic of the semiconductor (In_2O_3) and metal (Ni) junction band alignment. A negative Schottky barrier is formed. (c) Temperature-dependent transfer characteristics of an In_2O_3 FET. Gate leakage current is shown in a dashed line. (d) Temperature-dependent threshold voltage and field-effect mobility extracted from (c). (e) Arrhenius plot at different gate biases extracted from (c). Dashed lines fit linearly with the first six points. (f) Extracted contact barrier height Φ_B at various gate biases, showing a negative Schottky barrier.

The interface accumulation in In_2O_3 also improves the contact of the TFTs. Fig. 3(b) shows the band alignment of a semiconductor (In_2O_3) to metal (Ni) junction, where Q_{ss} is the interface trap charge, Q_{sc} is the space charge in

Authorized licensed use limited to: Purdue University. Downloaded on April 29,2024 at 17:42:21 UTC from IEEE Xplore. Restrictions apply.

semiconductor, and ϕ_{Bn0} is the barrier height. The barrier heights of metal–semiconductor junctions are determined by both the metal work function and the interface states. Due to the charge balance and the positively charged interface trap, negative space charges in blue will be present inside the channel, giving rise to the negative Schottky barrier. Normally, a positive Schottky barrier will form at the contact because of the Fermi-level pinning inside the bandgap. The electrons require thermal activation to be injected into the channel, thus resulting in a high contact resistance. Here, in In_2O_3, a negative Schottky barrier is formed due to the surface accumulation, making electrons flow freely between contact and channel. Again, the electron-accumulation-induced negative Schottky barrier in In_2O_3 greatly contrasts to conventional semiconductors, such as Si and III–V (except for InAs), whose interfaces have positive Schottky barriers and depletion regions.

In experiments, the Schottky barrier can be measured from temperature-dependent transfer and output characteristics. The current I_{DS} thermally injected from the contact is given by

$$I_{\mathrm{D}} = A^*_{2\mathrm{D}} T^{1.5} \exp\left(-\frac{\Phi_B}{k_B T}\right) \tag{1}$$

where $A^*_{2\mathrm{D}}$ is the Richardson constant, T is the temperature, k_B is Boltzmann's constant, and Φ_B is the effective barrier height. The temperature-dependent transfer curves of a 1-μm-long channel device with a channel thickness of 2.5 nm from 295 to 33 K are plotted in Fig. 3(c). The black dashed line indicates the gate leakage current. As shown in Fig. 3(d), the threshold voltage continuously shifted to positive when the temperature cooled. The field-effect mobility extracted from Fig. 3(c) shows a weak temperature dependence. The effective barrier height at a given V_{GS} can be extracted by plotting the Arrhenius plot [$\ln(I_{\mathrm{D}}/T^{1.5})$ versus $1/T$], shown in Fig. 3(e). At relatively high temperatures (from 295 to 150 K), the data are linear with a slope, which is negative at lower gate voltages and positive at higher gate voltages. The gate-dependent barrier height can then be calculated using (1), as shown in Fig. 3(f). Both short and long channel devices were measured. The flat band condition can be found when the gate-dependent barrier height deviates from a linear dispersion. The Schottky barrier is determined to be negative in In_2O_3 TFTs. In a short-channel device with L_{ch} of 40 nm, the negative contact barrier height is observed at all gate biases. It is worth mentioning that (1) is based on the thermal emission of electrons over a barrier, which is no longer valid when the barrier height is negative. However, the deviation from linear relation at lower temperature and the positive slope in Arrhenius plot indicate the negative Schottky barrier.

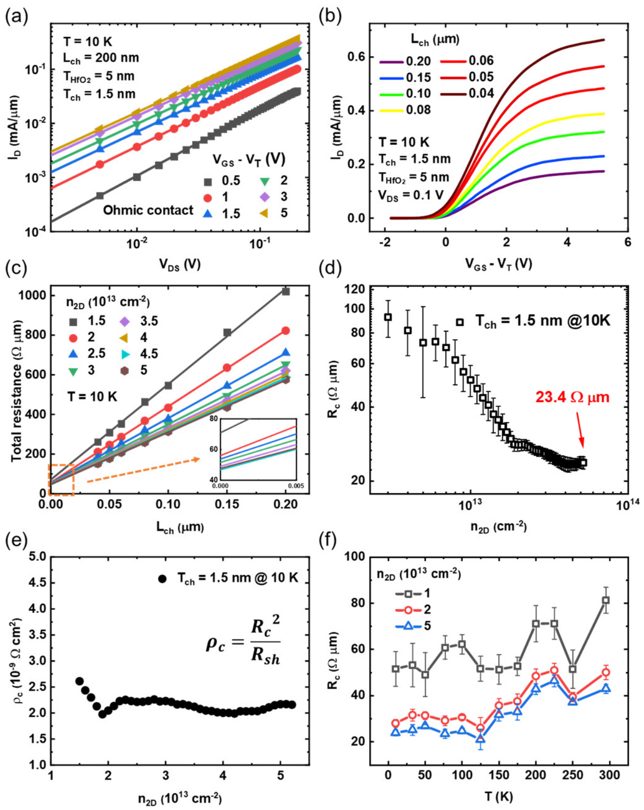

Fig. 4. (a) Logarithmic plot of the I_{D}–V_{DS} curve at different V_{GS}–V_T. The linear fitting shows excellent ohmic contact at 10 K. (b) Channel length L_{ch} dependence of the transfer curves at 10 K. (c) Contact resistance R_c extraction at different carrier densities by the TLM method. Inset: magnified plot showing the intercepts. (d) Carrier density dependence of the contact resistance R_c. (e) Contact resistivity ρ_c as a function of the carrier density. (f) Temperature dependence of the contact resistance R_c at different carrier densities.

Excellent ohmic contact is observed at various carrier densities even at a low temperature of 10 K, as shown in Fig. 4(a). This provides another evidence for the negative Schottky contact barrier in In_2O_3. Fig. 4(b) shows the channel-length-dependent transfer characteristics in a 1.5-nm-thick In_2O_3 film. The total resistance versus channel length is plotted and linearly fitted in Fig. 4(c) at 10 K. Using the transfer-length method (TLM), the carrier density $n_{2\text{-D}}$ dependence of sheet resistance R_{sh} and contact resistance R_c can be extracted from the slope and the intercept, respectively. The carrier density $n_{2\text{-D}}$ is estimated using

$$n_{2\mathrm{D}} = \frac{C_{\mathrm{ox}}(V_{\mathrm{GS}} - V_T)}{q} \tag{2}$$

where q is the elementary charge, C_{ox} is the normalized gate capacitance, which is experimentally measured to be 1.6×10^{-6} F/cm^2 for 5-nm HfO_2 in a capacitor with the same device structure (Ni/HfO_2/In_2O_3/Ni). Fig. 4(c) inset shows the enlarged intercept, indicating a small contact resistance. In ohmic contacts, if we consider a fully transparent junction with ballistic transport from metal to semiconductor, the contact resistance R_c is limited by the number of modes inside the semiconductor channel ($M = Wk_F/\pi$, where k_F is the Fermi vector and W is the width), where each mode contributes a conductance of $G_0 = 2e^2/h$ (2 is the spin degeneracy and h is the Planck constant). In single crystals, $k_F = (2\pi n_{2\mathrm{D}})^{1/2}$ without valley degeneracy. Fig. 4(d) shows the carrier density dependence of the contact resistance in a 1.5-nm-thick In_2O_3 film. Our devices have an ultralow contact resistance of 23.4 $\Omega\,\mu$m, pushing it toward the Landauer quantum limit. However, the carrier density could be underestimated, because the negative Schottky barrier will induce extra carriers at the contact. In addition, the ALD-grown In_2O_3 is amorphous,

Authorized licensed use limited to: Purdue University. Downloaded on April 29,2024 at 17:42:21 UTC from IEEE Xplore. Restrictions apply.

where the disordered structure induced extra localization and extended states, which is different from single crystals. The surface roughness can also influence the contact. The potential emergence of a secondary band, attributed to confinement in the out-of-plane direction at high carrier densities, may introduce additional modes within the In_2O_3 channel, consequently reducing the contact resistance limit. Further discussion on this phenomenon, along with theoretical calculations, will be presented in the last part of this section. The contact resistivity ρ_c is calculated from: $\rho_c = R_c^2/R_{\text{sh}}$ when $L_c \gg L_T$, where L_c is the contact length and L_T is the current transfer length. The contact resistivity shown in Fig. 4(e) has small dependence on the carrier density, indicating a transparent contact. The temperature dependence of contact resistance at three different carrier densities is shown in Fig. 4(f). The contact resistance decreases at low temperatures. In contrast to the positive Schottky barrier, where the current originates from the thermal emission of electrons overcoming the contact barrier, the contact resistance is highly temperature-dependent and increases notably at low temperatures. This result further confirms the previous conclusion of the surface-accumulation induced negative Schottky barrier concept and low temperature improves the contact in In_2O_3 TFTs.

The surface accumulation can be tuned by the post O_2 annealing of the devices, since the interfacial traps mainly originated from the oxygen vacancies. Fig. 5(a) describes the band alignment change at the contact after annealing: the CNL E_{CNL} drops, resulting in an increased barrier height or less negative barrier height. The surface accumulation change is also reflected in the positively shifted threshold voltage in Fig. 5(b). Fig. 5(c) shows the carrier density dependence of the contact resistance at different annealing temperatures (from as fabricated to 400 °C). The contact resistance increases at the same carrier density due to the less negative barrier height. Fig. 5(d) shows the effect of channel thickness on the surface accumulation. The threshold voltage shifted positively when the channel thickness thinned down to 1 nm. From the TLM method, the carrier density dependence of sheet resistance is calculated in Fig. 5(e). The sheet resistance increased at thinner films because of the increased surface roughness and the disorder-induced mobility drop. The current transfer length characterized the scale of the contact metal is estimated using: $L_T = R_c/R_{\text{sh}}$. Fig. 5(f) shows the film thickness dependence of contact resistivity and current transfer length. Extremely small contact resistivity of $\rho_c \approx 1.3 \times 10^{-9}\ \Omega\,\text{cm}^2$ and current transfer length of $L_T \approx 2$ nm are achieved in the 1-nm-thick In_2O_3 TFTs at room temperature, establishing an excellent foundation for the development of ultra-scaled In_2O_3 TFT technology for BEOL integration.

Fig. 6 is the benchmark of the contact resistance as a function of carrier density of In_2O_3 TFTs with other semiconductors [22], [23], [24], [25], [26], [27], [28], [29], [30], [31], [32], including Si, III–V, transition-metal dichalcogenides (TMDs), and amorphous oxides. This work demonstrates the smallest contact resistance, pushing it toward the Landauer quantum limit. We observed, for the first time in an In_2O_3 film, the surface-accumulation-induced negative Schottky barrier contact, which led to the near quantum-limit contact resistance.

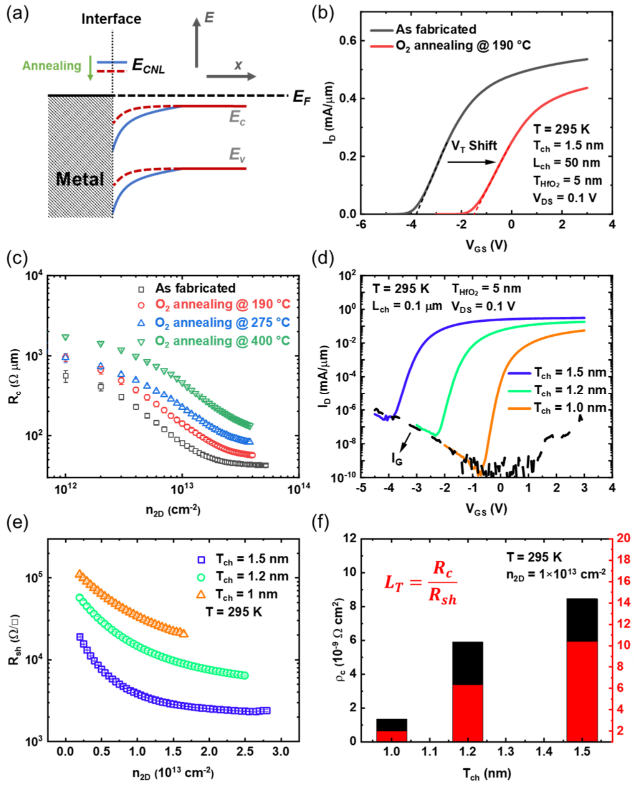

Fig. 5. (a) Model of contact band alignment after O_2 annealing. The decrease of positive charges at the interface lower the carrier density of the In_2O_3. (b) Transfer characteristics of an In_2O_3 FET after O_2 annealing. The threshold voltage V_T shifts positively. (c) Carrier density dependence of the contact resistance R_c at different O_2 annealing temperatures. (d) Transfer characteristics of In_2O_3 FETs with different channel thicknesses T_{ch}. Gate leakage current is shown as a dashed line. (e) Carrier-density-dependent sheet resistance R_{sh} at various channel thicknesses extracted from the TLM method. (f) Channel thickness dependence of the contact resistivity ρ_c and current transfer length L_T.

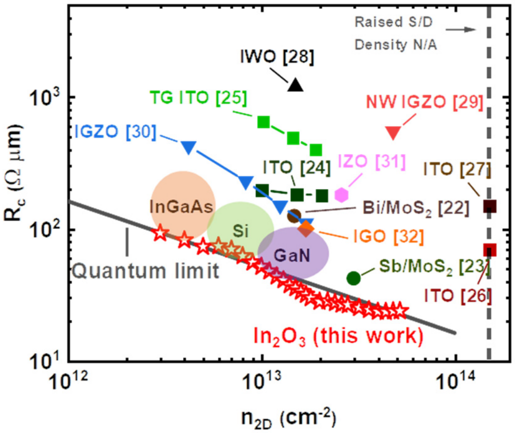

Fig. 6. Benchmark of contact resistance as a function of carrier density for semiconductors (III–V, Si, MoS_2, and amorphous oxides). This work shows the smallest contact resistance.

Using DFT, we calculate the lower limit contact resistance of nanometer thin In_2O_3. For a 2-D material, the lower limit contact resistance (for a single contact), R_c^{limit}, commonly referred to as the quantum limit, is equal to half of the

Authorized licensed use limited to: Purdue University. Downloaded on April 29,2024 at 17:42:21 UTC from IEEE Xplore. Restrictions apply.

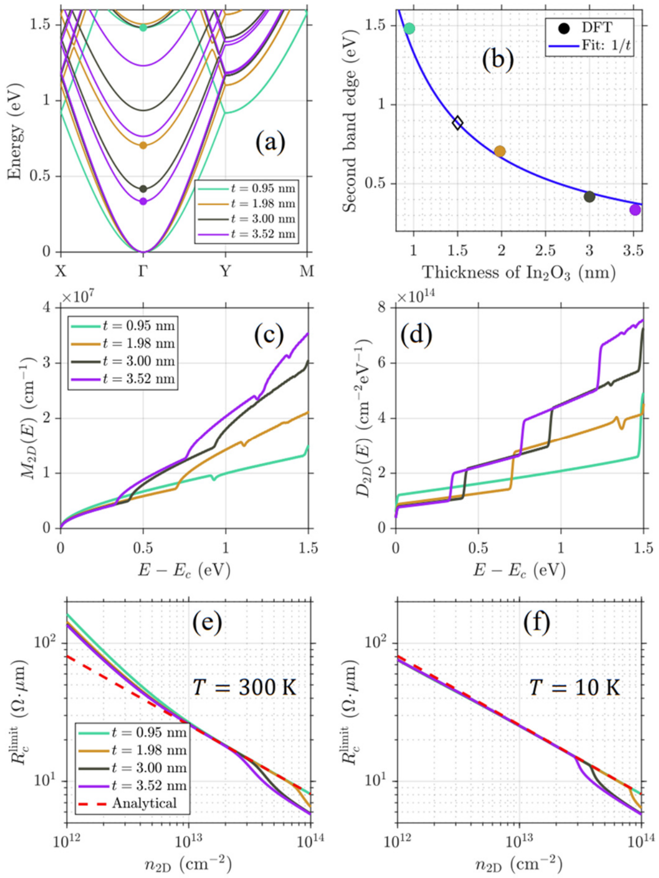

Fig. 7. DFT simulations of In_2O_3 films of thickness (t) equal to 0.95, 1.98, 3.00, and 3.52 nm. (a) Band structure along high-symmetry **k**-points. (b) Location of secondary band edge versus In_2O_3 thickness with $1/t$ fit. Open diamond marker is estimated value from fit for $t = 1.5$ nm. (c) Distribution of modes and (d) density of states versus energy relative to conduction band edge. (e) and (f) Lower limit contact resistance versus electron density at 300 and 10 K.

reciprocal of the ballistic conductance [33], [34]

$$\left(R_c^{\text{limit}}\right)^{-1} = \left(\frac{4e^2}{h}\right)\int_{-\infty}^{\infty} M_{\text{2-D}}(E)\left[-\frac{\partial f_0}{\partial E}\right]dE \tag{3}$$

where $M_{\text{2-D}}(E)$ is the 2-D distribution of modes, f_0 is the Fermi–Dirac distribution, and $2e^2/h$ is the quantum of conductance. A factor of two is included in (3) to account for the total contact resistance being split equally among both contacts by the simplest assumption. The only material-specific quantity in (3) is the 2-D distribution of modes, which is calculated using [35]

$$M_{\text{2-D}}(E) = \left(\frac{h}{2A}\right)\sum_{\mathbf{k},n}|v_x(\mathbf{k},n)|\delta(E - E_{\mathbf{k},n}) \tag{4}$$

where $\mathbf{k}$ is the electron wavevector (restricted to the first Brillouin zone), n is the band index, $E_{\mathbf{k},n}$ is the electron eigenenergy, $v_x(\mathbf{k},n) = (1/\hbar)\partial E_{\mathbf{k},n}/\partial k_x$ is the band velocity along the transport direction (assumed along x), and A is the area of the 2-D sample. The DFT-computed electron dispersion is used to obtain $M_{\text{2-D}}(E)$ and R_c^{limit}, as previously done with 2-D semiconductors [36], [37].

Fig. 7(a) shows the band structures of the four In_2O_3 nanometer thin films, with each displaying a single Γ-centered conduction band. The effective mass increases as the film thickness decreases: 0.19 m_0 with the 3.52- and 3.00-nm films, 0.23 m_0 with the 1.98-nm film, and 0.30 m_0 with the 0.95-nm film. The secondary band edge energies [labeled with filled circles in Fig. 7(a)] are found to follow a simple $1/t$ trend, where t is the film thickness [see Fig. 7(b)]. The 2-D distribution of modes versus energy is presented in Fig. 7(c). Near the conduction band edge, $M_{\text{2-D}}(E)$ scales as the square root of energy. This is expected since the distribution of modes for an isotropic 2-D parabolic band [38] is $M_{\text{2-D}}(E) = g_v(2m^*(E - E_c))^{1/2}/\pi\hbar$, where g_v is the valley degeneracy, or $M_{\text{2-D}}(k) = g_v k/\pi$ when expressed in terms of wavevector. There are distinct upticks in $M_{\text{2-D}}(E)$ that coincide with the additional contribution from higher energy secondary bands. The density of states, shown in Fig. 7(d), has step increases with the addition of each band. This is consistent with the expression for a 2-D effective mass band, $D_{\text{2-D}}(E) = g_v m^*/\pi\hbar^2$. Due to the nonparabolicity of the electron dispersion, the density of states increases linearly with energy away from the band edge.

Next, we calculate R_c^{limit} from the distribution of modes using (3) and we compute the 2-D electron density from the density of states using $n_{\text{2-D}} = \int_{E_c}^{\infty} D_{\text{2-D}}(E) f_0(E) dE$. Fig. 7(e) presents the lower limit contact resistance versus electron density at $T = 300$ K. As expected, R_c^{limit} decreases with increasing $n_{\text{2-D}}$. The results are nearly identical for all four In_2O_3 thicknesses, except at higher electron densities (above 3×10^{13} cm^{-2}), where a drop in R_c^{limit} is observed at different $n_{\text{2-D}}$. This sudden decrease in contact resistance occurs when the secondary band falls within the conduction window, $-\partial f_0/\partial E$, leading to an enhancement in $M_{\text{2-D}}(E)$. As a result, the drop in R_c^{limit} happens in order of the secondary band edge energy, which scales inversely with In_2O_3 film thickness.

To better understand the results, we can compare the DFT-computed R_c^{limit} to that of an analytical expression assuming a 2-D effective mass band in the low-temperature limit. At low temperature, $-\partial f_0/\partial E \approx \delta(E - E_F)$ and $f_0 \approx 1 - \theta(E - E_F)$, where $\delta(E)$ is a Dirac delta function and $\theta(E)$ is a Heaviside step function. Using these approximations to evaluate R_c^{limit} and $n_{\text{2-D}}$, in combination with the parabolic-band formulas for $M_{\text{2-D}}(E)$ and $D_{\text{2-D}}(E)$, we find $(R_c^{\text{limit}})^{-1} = g_v(4e^2/h)(2m^*(E_F - E_c))^{1/2}/\pi\hbar = g_v(4e^2/h)k_F/\pi$ and $n_{\text{2-D}} = g_v m^*(E_F - E_c)/\pi\hbar^2 = g_v k_F^2/2\pi$. When combined, this gives

$$R_c^{\text{limit}} = \frac{1}{\sqrt{g_v}}\frac{h}{4e^2}\sqrt{\frac{\pi}{2n_{\text{2-D}}}}. \tag{5}$$

This expression also applies in the limit of a degenerately doped semiconductor. This analytical formula, and variations of it, is commonly used to establish the lower limit contact resistance [22], [23]. It is common to find twice the value of (5) being adopted as the lowest quantum limit, but it is important to note that this would correspond to the lowest limit of the total contact resistance (due to both contacts with the equal resistance value as the simplest assumption, as opposed to a single contact).

Authorized licensed use limited to: Purdue University. Downloaded on April 29,2024 at 17:42:21 UTC from IEEE Xplore. Restrictions apply.

The analytical form of the lower limit contact resistance, with $g_v = 1$, is plotted as a red dashed line in Fig. 7(e). It is worth noting that the lower Landauer quantum limit for electron contact is expected with TMDs, such as MoS_2 with valley degeneracy $g_v = 2$. The DFT-computed and analytical curves agree for electron densities greater than 10^{13} cm^{-2}, where the degenerate limit is valid, but disagree once the secondary band enters the conduction window leading to a drop in R_c^{limit} (the analytical curve misses this feature since it assumes a single band). When calculating R_c^{limit} at $T = 10$ K [see Fig. 7(f)], where the low-temperature limit is more accurate, the DFT and analytical results agree over a wider electron concentration range, until the higher energy band comes into play.

When compared to the measured contact resistance at 10 K [Fig. 4(d)], the empirical R_c displays a dip at 2×10^{13} cm^{-2} that resembles the drop in R_c^{limit} due to the secondary band. From Fig. 7(b), the second band edge for a $t = 1.5$ nm In_2O_3 film is estimated to be 0.89 eV above the first band edge (shown as open symbol). According to our calculation, this would produce a dip in R_c^{limit} at roughly 1.5×10^{14} cm^{-2}. The lower $n_{\text{2-D}}$ at which the dip is observed could be the result of disorder-induced band structure change due to the amorphous nature of the ALD-grown In_2O_3 film.

IV. CONCLUSION

In summary, this study demonstrates the impressive electrical performance of ALD-grown In_2O_3 TFTs with BEOL compatibility at both room temperature (295 K) and low temperature (10 K). A good contact is the precondition of a good transistor. The excellent ohmic contact with ultralow contact resistance $R_c = 23.4\ \Omega\,\mu$m at $n_{2D} = 5.0 \times 10^{13}$ cm^{-2} is achieved due to the negative Schottky barrier induced by surface accumulation in In_2O_3. Together with the theoretical calculation, the quantum limit of metal to semiconductor contact resistance is discussed. The effect of annealing and channel thickness on contact resistance is experimentally investigated. Notably, ultralow contact resistivity $\rho_c \approx 1.3 \times 10^{-9}\ \Omega\,\text{cm}^2$ and current transfer length $L_T \approx 2$ nm are achieved in a 1-nm-thick film. These findings provide a strong foundation from the contact engineering point of view for considering ALD In_2O_3 as a promising BEOL oxide semiconductor channel material for next-generation high-performance ultra-scaled BEOL electronics. It is also worth noting all the methodology developed in this work is also valid for InAs [39] and InN, whose CNL is also deeply aligned inside the conduction band in these materials.

REFERENCES

[1] K. Nomura, A. Takagi, T. Kamiya, H. Ohta, M. Hirano, and H. Hosono, "Amorphous oxide semiconductors for high-performance flexible thin-film transistors," *Jpn. J. Appl. Phys.*, vol. 45, no. 5, p. 4303, May 2006, doi: 10.1143/jjap.45.4303.

[2] T. Kamiya, K. Nomura, and H. Hosono, "Present status of amorphous In-Ga-Zn-O thin-film transistors," *Sci. Technol. Adv. Mater.*, vol. 11, no. 4, Feb. 2010, Art. no. 044305, doi: 10.1088/1468-6996/11/4/044305.

[3] H. Yabuta et al., "High-mobility thin-film transistor with amorphous InGaZnO4 channel fabricated by room temperature RF-magnetron sputtering," *Appl. Phys. Lett.*, vol. 89, no. 11, Sep. 2006, Art. no. 112123, doi: 10.1063/1.2353811.

[4] I.-H. Baek et al., "High-performance thin-film transistors of quaternary indium-zinc-tin oxide films grown by atomic layer deposition," *ACS Appl. Mater. Interface*, vol. 11, no. 16, pp. 14892–14901, Apr. 2019, doi: 10.1021/acsami.9b03331.

[5] H. Salami, A. Uy, A. Vadapalli, C. Grob, V. Dwivedi, and R. A. Adomaitis, "Atomic layer deposition of ultrathin indium oxide and indium tin oxide films using a trimethylindium, tetrakis(dimethylamino)tin, and ozone precursor system," *J. Vac. Sci. Technol. A, Vac., Surf., Films*, vol. 37, no. 1, Jan. 2019, Art. no. 010905, doi: 10.1116/1.5058171.

[6] C. R. Allemang et al., "High-performance zinc tin oxide TFTs with active layers deposited by atomic layer deposition," *Adv. Electron. Mater.*, vol. 6, no. 7, Jul. 2020, Art. no. 2000195, doi: 10.1002/aelm.202000195.

[7] H. Kim et al., "Indium tin oxide thin films for organic light-emitting devices," *Appl. Phys. Lett.*, vol. 74, no. 23, pp. 3444–3446, Jun. 1999, doi: 10.1063/1.124122.

[8] A. Nathan, S. Lee, S. Jeon, and J. Robertson, "Amorphous oxide semiconductor TFTs for displays and imaging," *IEEE/OSA J. Display Technol.*, vol. 10, no. 11, pp. 917–927, Nov. 2014, doi: 10.1109/JDT.2013.2292580.

[9] H.-I. Yeom, J. B. Ko, G. Mun, and S.-H.-K. Park, "High mobility polycrystalline indium oxide thin-film transistors by means of plasma-enhanced atomic layer deposition," *J. Mater. Chem. C*, vol. 4, no. 28, pp. 6873–6880, 2016, doi: 10.1039/c6tc00580b.

[10] J. Lee et al., "High mobility ultra-thin crystalline indium oxide thin film transistor using atomic layer deposition," *Appl. Phys. Lett.*, vol. 113, no. 11, Sep. 2018, Art. no. 112102, doi: 10.1063/1.5041029.

[11] M. Si, Z. Lin, Z. Chen, X. Sun, H. Wang, and P. D. Ye, "Scaled indium oxide transistors fabricated using atomic layer deposition," *Nature Electron.*, vol. 5, no. 3, pp. 164–170, Feb. 2022, doi: 10.1038/s41928-022-00718-w.

[12] A. Charnas, Z. Lin, Z. Zhang, and P. D. Ye, "Atomically thin In_2O_3 field-effect transistors with 1017 current on/off ratio," *Appl. Phys. Lett.*, vol. 119, no. 26, Dec. 2021, doi: 10.1063/5.0075166.

[13] Z. Zhang et al., "A gate-all-around inO nanoribbon FET with near 20 mA/m drain current," *IEEE Electron Device Lett.*, vol. 43, no. 11, pp. 1905–1908, Nov. 2022, doi: 10.1109/LED.2022.3210005.

[14] Z. Lin et al., "Nanometer-thick oxide semiconductor transistor with ultra-high drain current," *ACS Nano*, vol. 16, no. 12, pp. 21536–21545, Dec. 2022, doi: 10.1021/acsnano.2c10383.

[15] Z. Zhang, Z. Lin, C. Niu, M. Si, M. A. Alam, and P. D. Ye, "Ultrahigh bias stability of ALD In_2O_3 FETs enabled by high temperature O_2 annealing," in *Proc. IEEE Symp. VLSI Technol. Circuits (VLSI Technol. Circuits)*, Kyoto, Japan, Jun. 2023, pp. 1–2, doi: 10.23919/vlsitechnologyandcir57934.2023.10185292.

[16] P. D. C. King, T. D. Veal, D. J. Payne, A. Bourlange, R. G. Egdell, and C. F. McConville, "Surface electron accumulation and the charge neutrality level in In_2O_3," *Phys. Rev. Lett.*, vol. 101, no. 11, Sep. 2008, Art. no. 116808, doi: 10.1103/physrevlett.101.116808.

[17] J. Guo and M. S. Lundstrom, "A computational study of thin-body, double-gate, Schottky barrier MOSFETs," *IEEE Trans. Electron Devices*, vol. 49, no. 11, pp. 1897–1902, Nov. 2002, doi: 10.1109/TED.2002.804696.

[18] P. Giannozzi et al., "Advanced capabilities for materials modelling with quantum ESPRESSO," *J. Phys., Condens. Matter*, vol. 29, no. 46, Nov. 2017, Art. no. 465901, doi: 10.1088/1361-648x/aa8f79.

[19] J. P. Perdew, K. Burke, and M. Ernzerhof, "Generalized gradient approximation made simple," *Phys. Rev. Lett.*, vol. 77, no. 18, pp. 3865–3868, Oct. 1996, doi: 10.1103/PhysRevLett.77.3865.

[20] D. R. Hamann, "Optimized norm-conserving Vanderbilt pseudopotentials," *Phys. Rev. B, Condens. Matter*, vol. 88, no. 8, Aug. 2013, Art. no. 085117, doi: 10.1103/PhysRevB.88.085117.

[21] A. A. Mostofi et al., "An updated version of wannier90: A tool for obtaining maximally-localised wannier functions," *Comput. Phys. Commun.*, vol. 185, no. 8, pp. 2309–2310, Aug. 2014, doi: 10.1016/j.cpc.2014.05.003.

[22] P.-C. Shen et al., "Ultralow contact resistance between semimetal and monolayer semiconductors," *Nature*, vol. 593, no. 7858, pp. 211–217, May 2021, doi: 10.1038/s41586-021-03472-9.

[23] W. Li et al., "Approaching the quantum limit in two-dimensional semiconductor contacts," *Nature*, vol. 613, no. 7943, pp. 274–279, Jan. 2023, doi: 10.1038/s41586-022-05431-4.

Authorized licensed use limited to: Purdue University. Downloaded on April 29,2024 at 17:42:21 UTC from IEEE Xplore. Restrictions apply.

[24] C. Gu et al., “High-performance short-channel top-gate indium-tin-oxide transistors by optimized gate dielectric,” *IEEE Electron Device Lett.*, vol. 44, no. 5, pp. 837–840, May 2023, doi: 10.1109/LED.2023.3262684.

[25] L. Hoang et al., “Bias stress stability of ITO transistors and its dependence on dielectric properties,” in *Proc. Device Res. Conf. (DRC)*, Columbus, OH, USA, Jun. 2022, pp. 1–2, doi: 10.1109/DRC55272.2022.9855789.

[26] Y. Kang, K. Han, Y. Chen, and X. Gong, “Thickness-engineered extremely-thin channel high performance ITO TFTs with raised S/D architecture: Record-low RSD, highest moblity (sub-4 nm TCH regime), and high VTH tunability,” in *Proc. IEEE Symp. VLSI Technol. Circuits (VLSI Technol. Circuits)*, Kyoto, Japan, Jun. 2023, pp. 1–2, doi: 10.23919/VLSITechnologyandCir57934.2023.10185421.

[27] M. Si et al., “Indium-tin-oxide transistors with one nanometer thick channel and ferroelectric gating,” *ACS Nano*, vol. 14, no. 9, p. 11542, Aug. 2020, doi: 10.1021/acsnano.0c03978.

[28] W. Chakraborty, B. Grisafe, H. Ye, I. Lightcap, K. Ni, and S. Datta, “BEOL compatible dual-gate ultra thin-body W-doped indium-oxide transistor with ion = 370μA/μm, SS = 73 mV/dec and ion /Ioff ratio $> 4 \times 109$,” in *Proc. IEEE Symp. VLSI Technol.*, Honolulu, HI, USA, Jun. 2020, pp. 1–2, doi: 10.1109/VLSITechnology18217.2020.9265064.

[29] K. Han et al., “Indium-gallium-zinc-oxide (IGZO) nanowire transistors,” *IEEE Trans. Electron Devices*, vol. 68, no. 12, pp. 6610–6616, Dec. 2021, doi: 10.1109/TED.2021.3113893.

[30] J. Zhang et al., “First demonstration of BEOL-compatible atomic-layer-deposited InGaZnO TFTs with 1.5 nm channel thickness and 60 nm channel length achieving ON/OFF ratio exceeding 10^{11}, SS of 68 mV/dec, normal-off operation and high positive gate bias stability,” in *Proc. IEEE Symp. VLSI Technol. Circuits (VLSI Technol. Circuits)*, Jun. 2023, pp. 1–2, doi: 10.23919/VLSITechnologyand-Cir57934.2023.10185312.

[31] Y.-K. Liang et al., “Electrical characteristics of ultrathin InZnO thin-film transistors prepared by atomic layer deposition,” *IEEE Trans. Electron Devices*, vol. 70, no. 3, pp. 1067–1072, Mar. 2023, doi: 10.1109/TED.2022.3232476.

[32] J. Zhang, D. Zheng, Z. Zhang, A. Charnas, Z. Lin, and P. D. Ye, “Ultrathin InGaO thin film transistors by atomic layer deposition,” *IEEE Electron Device Lett.*, vol. 44, no. 2, pp. 273–276, Feb. 2023, doi: 10.1109/LED.2022.3233080.

[33] J. Maassen, C. Jeong, A. Baraskar, M. Rodwell, and M. Lundstrom, “Full band calculations of the intrinsic lower limit of contact resistivity,” *Appl. Phys. Lett.*, vol. 102, no. 11, Mar. 2013, Art. no. 111605, doi: 10.1063/1.4798238.

[34] S. Datta, *Electronic Transport in Mesoscopic Systems*. New York, NY, USA: Cambridge Univ. Press, 1995.

[35] C. Jeong, R. Kim, M. Luisier, S. Datta, and M. Lundstrom, “On Landauer versus Boltzmann and full band versus effective mass evaluation of thermoelectric transport coefficients,” *J. Appl. Phys.*, vol. 107, no. 2, Jan. 2010, Art. no. 023707, doi: 10.1063/1.3291120.

[36] V. Mishra and S. Salahuddin, “Intrinsic limits to contact resistivity in transition metal dichalcogenides,” *IEEE Electron Device Lett.*, vol. 38, no. 12, pp. 1755–1758, Dec. 2017, doi: 10.1109/LED.2017.2762158.

[37] S. V. Suryavanshi et al., “Improving electric contacts to two-dimensional semiconductors,” 2021, *arXiv:2105.10792*.

[38] R. Kim, S. Datta, and M. S. Lundstrom, “Influence of dimensionality on thermoelectric device performance,” *J. Appl. Phys.*, vol. 105, no. 3, Feb. 2009, Art. no. 034506, doi: 10.1063/1.3074347.

[39] K. Sumita, J. Takeyasu, K. Toprasertpong, M. Takenaka, and S. Takagi, “Low specific contact resistance between InAs/Ni-InAs evaluated by multi-sidewall TLM,” *AIP Adv.*, vol. 13, no. 5, May 2023, Art. no. 055310, doi: 10.1063/5.0150296.

Authorized licensed use limited to: Purdue University. Downloaded on April 29,2024 at 17:42:21 UTC from IEEE Xplore. Restrictions apply.